Effect of cycling on ultra-thin $HfZrO_4$, ferroelectric synaptic weights

NEUROMORPHIC
Computing and Engineering

PAPER

Effect of cycling on ultra-thin $HfZrO_4$, ferroelectric synaptic weights

Laura Bégon-Lours[1,*], **Mattia Halter**[1,2], **Marilyne Sousa**[1], **Youri Popoff**[1,2], **Diana Dávila Pineda**[1], **Donato Francesco Falcone**[1], **Zhenming Yu**[1,3,5], **Steffen Reidt**[1], **Lorenzo Benatti**[4], **Francesco Maria Puglisi**[4] and **Bert Jan Offrein**[1]

[1] IBM Research Europe—Zurich Research Laboratory, Rüschlikon, Switzerland
[2] ETH Zurich—Integrated Systems Laboratory, Zurich, Switzerland
[3] Institute of Neuroinformatics, University of Zürich and ETH Zürich, Zürich, Switzerland
[4] UNIMORE—Dipartimento di Ingegneria 'Enzo Ferrari', 41125 Modena, Italy
[*] Author to whom any correspondence should be addressed.
[5] Current address: Forschungszentrum Jülich PGI-15, Aachen, Germany.

E-mail: lbe@zurich.ibm.com

Keywords: hafnium zirconate, ferroelectrics, synaptic weights

OPEN ACCESS

RECEIVED
10 November 2021

REVISED
23 February 2022

ACCEPTED FOR PUBLICATION
7 March 2022

PUBLISHED
25 March 2022

Abstract

Two-terminal ferroelectric synaptic weights are fabricated on silicon. The active layers consist of a 2 nm thick WO_x film and a 2.7 nm thick $HfZrO_4$ (HZO) film grown by atomic layer deposition. The ultra-thin HZO layer is crystallized in the ferroelectric phase using a millisecond flash at a temperature of only 500 °C, evidenced by x-rays diffraction and electron microscopy. The current density is increased by four orders of magnitude compared to weights based on a 5 nm thick HZO film. Potentiation and depression (analog resistive switching) is demonstrated using either pulses of constant duration (as short as 20 nanoseconds) and increasing amplitude, or pulses of constant amplitude (+/−1 V) and increasing duration. The cycle-to-cycle variation is below 1%. Temperature dependent electrical characterisation is performed on a series of device cycled up to 10^8 times: they reveal that HZO possess semiconducting properties. The fatigue leads to a decrease, in the high resistive state only, of the conductivity and of the activation energy.

1. Introduction

In artificial neural network accelerators [1, 2], the matrix-vector multiplication, or multiply and accumulate operation, is implemented using analog signals and weights by a parallel accumulation of currents generated across an array of reprogrammable resistances. The use of $HfZrO_4$ (HZO) [3] and more generally HfO_2-based ferroelectric compounds [4], receive increasing interest for analog, neuromorphic and in-memory computing. A concept of ferroelectric memristor is based on a ferroelectric layer separating two electrodes of a different material, thin enough to allow electrical conduction and thick enough to stabilize ferroelectricity. The energy profile of the device is modified upon polarization reversal, inducing the remanent modification of the resistance. Such electroresistance effect was first demonstrated using epitaxial ferroelectric perovskites [5–8], and recently using epitaxial thin films of the fluorite $HfZrO_4$ (HZO) [9, 10]. State-of-the-art double-layer polycrystalline HfO_2(10 nm)/Al_2O_3 junctions [11, 12] suffer from non-linear current–voltage characteristic (which can be circumvent by using a logarithmic driver [13]) and a relatively low current density (∼1 μA cm^{-2} at 2 V).

A direction towards larger current densities and linearity is to thin down the ferroelectric layer. Apart from epitaxial films deposited by pulsed laser deposition [9, 14] or sputtering [15], most films are deposited amorphous e.g. using molecular beam epitaxy [16] or atomic layer deposition (ALD) [3, 4], and subsequently annealed. The crystallisation of ultra-thin films is challenging because of the increased thermal budget required to obtain ferroelectricity as the thickness decreases [17]: using rapid thermal annealing, Liang *et al* required 600 °C for 5 nm thick HZO films and Ali *et al* as much as 800 °C for 4 nm. In this work, we reduce the thickness of HZO layer to only 2.7 nm, and use a millisecond flash lamp annealing technique, allowing thermalisation at only 500 °C.

Another limitation of ferroelectric tunnel junctions using a dielectric interlayer is the poor screening of the polarization charges by the later. In this work a transition metal oxide (WO_x) is used instead. At the cost of a reduced On/Off ratio, the 2.7 nm thick HZO layer enables the devices to operate at low bias (<100 mV), in a linear regime, with a large current density of 0.01 A cm^{-2} at 100 mV. Such a device operating in the quasi-ohmic regime was already demonstrated using 5 nm thick HZO films with WO_x [18] or TiO_x [19] interlayers: they have the advantage of back-end-of-line compatibility, but the current density was only 1 μA cm^{-2} at a read voltage of 100 mV. This work further establishes the depression/potentiation capability of ferroelectric, two-terminals synaptic weights.

2. Ultra-thin $HfZrO_4$ based devices

The process flow for the fabrication of the synaptic weights is summarized in figure 1(a). A 200 nm thick SiO_2 oxide was grown on Si by thermal oxidation. The active stack was then deposited by plasma-enhanced atomic layer deposition (PE-ALD): 20 nm of TiN is deposited at 300 °C with Tetrakis(dimethylamino)titanium and N_2 as precursors. 2 nm of WO_x is deposited at 375 °C with $(BuN)_2W(NMe_2)_2$ and O_2, then 3 nm of HZO is deposited at 300 °C alternating one cycle with Tetrakis(ethylmethylamino) hafnium (IV) and O_2, and two cycles with Bis (methylcyclopentadienyl) (methyl) (methoxy) zirconium (IV) and O_2. Ten additional nanometers of TiN are deposited as a capping layer to promote HZO crystallization in the ferroelectric phase during the annealing [20]. The choice of a stack fully deposited by ALD is motivated by the conformal character of the growth, which opens the door to future 3D integration, towards further reduction of the device footprint. In order to provide HZO with asymmetric interfaces while ensuring a maximal current density, the combination of an ultra-thin metal oxide interlayer and a metallic bottom electrode was preferred to a thick metal oxide electrode. TiO_x was first studied as a metal oxide interlayer: for 5 nm thick HZO synaptic weights, replacing TiO_x [19] by WO_x [18] resulted in a higher On/Off ratio and suppressed the need for a wake-up sequence, indicating that the HZO/metal oxide interface is active on the device characteristics such as On/Off ratio, rather than the bulk of the metal oxide. The crystallization was performed using the millisecond flash lamp annealing technique [21]: the sample was preheated to 500 °C, then a 20 ms long energy pulse of 90 J cm^{-2} was applied. The as-grown HZO layer was amorphous [21]. Although 400 °C was sufficient to crystallize 5 nm thick films [18], in this work films flash-annealed at 450 °C did not show any sign of crystallization. The increased temperature required as the thickness decreases was observed by Tahara *et al* [17] on TiN/HZO/TiN stacks. Thanks to the relatively thin top electrode, it is possible to measure the different layers thicknesses by x-ray reflectivity (HZO was found to be 2.7 nm thick) and to verify the crystallinity of the HZO layer using the grazing incidence x-ray diffraction technique (2θ scan at $\omega = 0.4°$), as shown in figure 1(b). A Bruker D8 Discover diffractometer equipped with a rotating anode generator was used. For comparison, the green lines (resp. purple) correspond to the monoclinic HZO (resp. tetragonal ZrO_2) in Materlik *et al* [22] and the orange lines to the orthorhombic HZO in Müller *et al* [23]. The peaks at $2\theta = 37°$ and 43° (CIF 1011102) show that TiN is polycrystalline. No monoclinic HZO is found: the peak observed at $2\theta = 30.5°$ matches the (111) planes of the orthorhombic phase. The peak is broad, which is not attributed to the presence of multiple peaks but to the reduced crystallite size. It is fitted by a Gaussian with a width at half maximum of $w = 2.5°$. The angle between the incident beam and the surface of the film was $\omega = 0.4°$. Using a k factor of 0.9, the crystallite size (along the direction that is 15° off the surface, approximately in-plane) was estimated using the Scherrer equation [24]: $d = k\lambda^{Cu}_{k\alpha 1}/(w \cos\theta)$ to be $d = 3.4$ nm. For comparison, this size is slightly larger than the thickness of the HZO layer. Bright-field high-resolution scanning transmission electron microscopy (BF-HRSTEM, double corrected JEOL ARM200F operated at 200 kV) was performed on a lamella prepared by focussed ion beam (FIB). Occasionally, wide grains (figure 2(a)) extend on several tens of nanometers. The images reveal a broad distribution of grain size (see figure 2(b)). The eventual small grains responsible for the XRD peak broadening cannot be observed due to the lamella's thickness. In addition, the images reveal a columnar growth of the bottom TiN electrode, causing a roughness of several nanometers that is transferred to the WO_x and HZO layers. The large grain in figure 2(a) was analysed closely (figure 2(c)); the lattice planes are oriented 69° off the surface of the film. The FFT (inset) estimates the interplanar distance to 0.30 nm. The planes are attributed to the {111} planes of the $Pca2_1$ unit cell, computed using Vesta [25] (figure 2(d)). The (11-1) planes are represented by the green line, their orientation correspond to a grain whose (634) planes would be parallel to the surface. The same analysis is performed for a grain from figure 2(b). The FFT in figure 2(e) reveals two families of perpendicular lattice planes distant of 0.15 nm and 0.18 nm. They are respectively attributed to the (13-1) and (202) planes, represented by the magenta and blue lines in figures 2(e) and (f). Remarkably, the grain appears to share the same out-of-plane orientation than the grain in figures 2(a) and (c). The mechanisms eventually correlating the grain size to the grain orientation are not explored in this work; a surface energy model of HZO was proposed by Materlik *et al* [22]. The WO_x remains amorphous after the annealing, as observed in figure 2(c). A 100 nm thick W metal electrode was then deposited by sputtering. The top electrode, defining

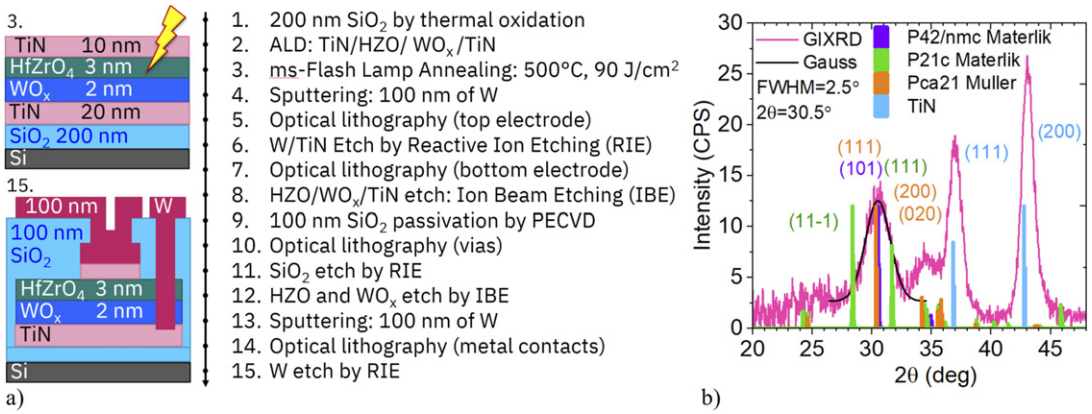

Figure 1. (a) Process-flow for the fabrication of ferroelectric memristors. At stage 3, a millisecond flash lamp annealing step is performed to crystallize the HZO layer, confirmed by (b) grazing incidence x-ray diffraction. No monoclinic HZO is found (grey reference peaks). After stage 15, the devices are finalized, a cross-section sketch is provided.

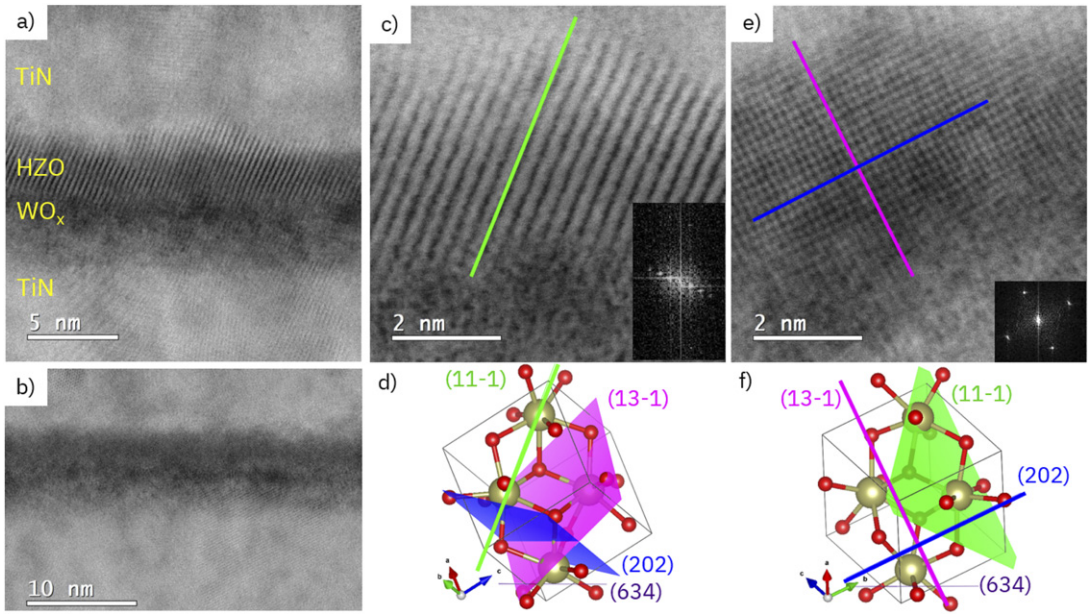

Figure 2. (a) and (b) BF-HRSTEM images of two wide grains (>10 nm). (c) Is a zoom in (a). The FFT (inset) is extracted from (c) and correspond to (11-1) lattice planes distant of $d = 0.30$ nm, represented by the green planes in (c) and (d). (e) Is a zoom in (b). The FFT is extracted from (e) and indicate a periodicity corresponding to (13-1) and (202) lattice planes distant of $d = 0.15$ nm and $d = 0.18$ nm, represented by the magenta and blue planes in (e) and (f). The $Pca2_1$ unit cell of HfO_2 in (d) and (f) is computed using Vesta and is represented normal to the (634) plane (purple line).

the area of the junction, was defined by optical lithography and reactive ion etching (RIE) of the W and top TiN layers. Using this method, the HZO layer acts as an etch stop. The bottom electrode was then defined by optical lithography and ion beam etching (IBE) of the HZO, WO_x and TiN layer, using a beam current of 150 mA. A 100 nm thick SiO_2 passivation layer was deposited at 300 °C by plasma-enhance chemical vapour deposition (PECVD). Vias to the top and the bottom electrode were defined by optical lithography. The SiO_2 layer was etched by RIE, then the HZO and the WO_x were etched by IBE, exposing the TiN layer to air. The etch was immediately followed by the sputtering of 100 nm of W. Metal contacts were then defined by optical lithography and etching. A schematic cross-section of the final device is found in figure 1(a).

3. Ferroelectric synaptic weights

The analog resistive switching properties of the devices are characterized. Both the programmability of the device for inference and its response under pulses of varying sign, amplitude and width are addressed, emulating—as proposed for example in [26] or [27]—the combination of pre-synaptic pulses (negative bias) and post-synaptic pulses (positive bias). The bottom (TiN/WO_x) electrode is grounded.

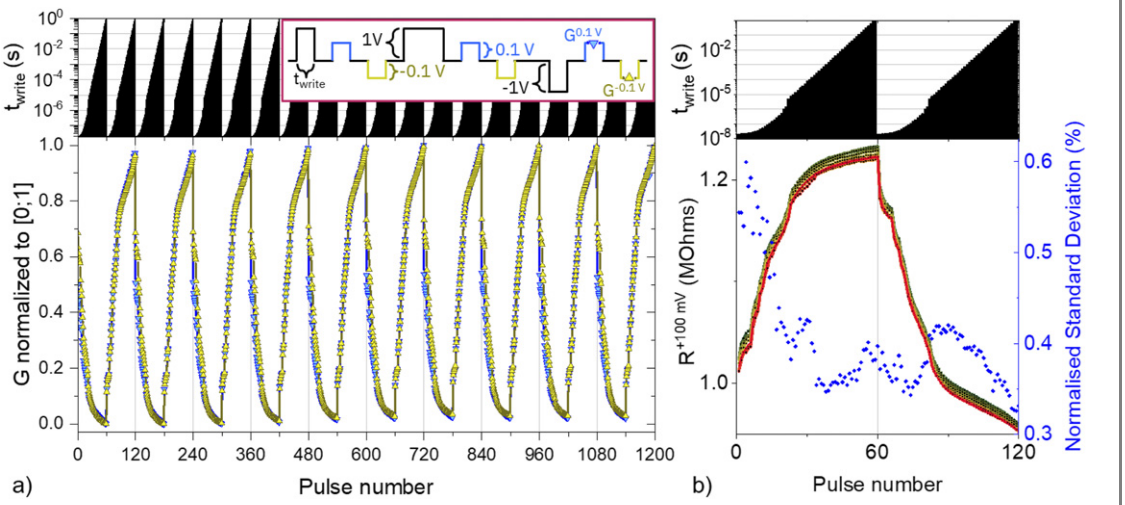

Figure 3. (a) Potentiation/depression cycles (40 μm device). The data is normalized to the [0; 1] range. Prior the test, the device is reset/set by applying a pulse of 1 V, 1 s followed by a pulse of −1 V, 1 s. After each pulse of amplitude $V_{write} = 1$ V (depression) or $V_{write} = -1$ V (potentiation) and increasing duration t_{write} (upper panel, from 20 ns to 1 s), the conductance of the synaptic weight is measured at 100 mV (blue data points) and then at −100 mV (yellow data points). The first to tenth cycles of the measured data are found in (b), where the green curve represents the resistance R^{+100mV} measured at 100 mV for pulses 1 to 120, and the red curve for 1081 to 1200. The blue data points (right axis) indicate the normalized standard deviation of R^{+100mV} over the ten cycles.

Prior to each test, the device was set by applying a pulse of 1 V, 1 s followed by a pulse of −1 V, 1 s. The measurement scheme is as follows: first, a pulse of amplitude V_{write} and duration t_{write} is applied using a B1530A waveform generator/fast measurement unit (WGFMU). The rise and fall time are set to 20 ns. Then, a B1500 analyser high-resolution source measurement unit is used to measure the conductance $G^{0.1V}$ of the device at a read bias of 100 mV. Keeping t_{write} constant, the write/read operation is repeated with a different V_{write}, as represented in figure 3: the arrows indicate the chronological order.

Electroresistance loops are measured for various t_{write}. The range of the amplitude is adapted in such a way that the saturation of the conductance is observed: it is +/−2.8 V for ultra-fast pulses of 20 ns, and +/−1 V for long pulses of 2 s. Such dynamics are consistent with the empirical Merz's law for the switching of ferroelectric domains [28]. Pulses of the same sign but with decreasing amplitude allow several micro-amperes to flow through the junction but only slightly modify the resistance (horizontal branches in the hysteresis loops, from 2.8 V to −0.8 V), showing that the resistive switching is field- and not current-driven, consistent with a resistive switching mechanism related to the ferroelectric domains switching. The remanent polarisation was measured by the positive up negative down (PUND) method: it is independent of the device area and is $2P_r = 2.25$ μC cm^{-2} at 500 kHz. This value is significantly lower than what is typically observed for 10 nm thick HZO (16 μC cm^{-2} [3]), and compares with the values measured by Chernikova *et al* in 2.5 nm thick films on TiN (2.5–3.5 μC cm^{-2} [29]). The small polarization in our films is not due to the presence of monoclinic grains (figure 1(b)). The presence of tetragonal grains in ultra-thin HZO films is typically associated to a wake-up effect, not measured in our devices [30]. A possible explanation can be the depolarization field (an effect more pronounced in ultra-thin films), typically responsible for a diminution of the ferroelectric polarization due to a finite screening length in the electrodes [31]. The presence of grains oriented along the [634] directions, discussed earlier, also contribute to the small polarization: in these grains, the projection of the polarization (which is parallel to the *c*-axis of the $Pca2_1$ unit cell) [22] along the normal to the surface is only 53% of its norm.

The proposed devices are energy efficient: 20 ns long pulses allow to update the synaptic weight with an energy in the pico-Joule range. The 'reading' operation at 100 mV would dissipates less than a femto-Joule for a reading time of the order of the micro-second.

Potentiation and depression is also obtained by keeping the amplitude V_{write} constant ($V_{write} = 1$ V for the depression and $V_{write} = -1$ V for the potentiation) and increasing the duration t_{write} (upper panel of figures 4(a) and (b)). Figure 3(a) shows the normalised conductance G of the device measured at 0.1 V (blue data points) and at −0.1 V (yellow data points) after each pulse of duration t_{write}. The sequence G^{-100mV} is larger than G^{+100mV} by a factor 2.5–2.7 due to a moderate diode-like character in the current–voltage characteristics. Two regimes are observed: below 10 μs, the conductance varies linearly with 10 to the power of t_{write}, and 20% of the dynamic range is covered by the first pulse (20 ns). Above 10 μs, the dependence is slower, which could involve effects other that ferroelectric domains switching such as reversible charged defects migration within

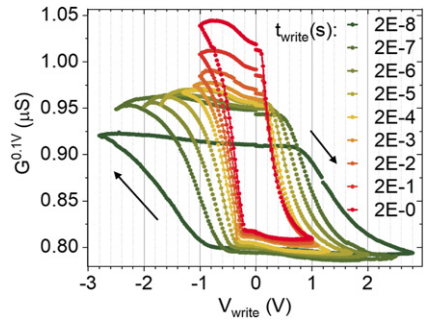

Figure 4. Conductance measured at 0.1 V after each pulse of duration t_{write} and amplitude V_{write}. The arrows indicate the chronological occurrence.

the layers. In figure 3(b), the resistance measured at 100 mV, $R^{+100\text{mV}} = 1/G^{+100\text{mV}}$ is represented as a function of the relative pulse number (green curve: first cycle, red curve: tenth cycle). In this representation the two regimes are also visible. For each pulse number, the normalised standard deviation (independently calculated from the conductance or from the resistance), or cycle-to-cycle variation, was measured: it is maximal after the first pulse where it is as low as 0.6%.

4. Effect of fatigue and temperature

Four devices are cycled respectively 10^5, 10^6, 10^7 and 10^8 times at +/−1 V, at a frequency of 100 kHz. Temperature dependent measurements are carried out on these four devices in addition to one in the pristine state. The five devices are in different fatigue states. After setting the temperature, the chip is thermalised for 15 min. The device is first set in the LRS by a DC sweep from 0 to −1 V, then a non-switching I–V sweep is performed from 0 to 80 mV. The current density $J+$ as a function of the voltage $V+$ (for the device with 10^2 cycles) is represented by the circles in figure 5(a). The device is then set in the HRS (DC sweep from 0 to 1 V) and measured (diamonds in figure 5(a)). In a first approximation, the transport for a positive bias on the top electrode is Ohmic. It is described by [32]:

$$\text{Log}\,(J) = \text{Log}\left(\frac{\mu q N_C}{t}\right) + \frac{-(E_C - E_F)}{k} \times \frac{1}{T} + \text{Log}(V)$$
$$J = \sigma E = \mu q N_C \exp\left(\frac{-(E_C - E_F)}{kT}\right) E, \quad (1)$$

where μ the electron mobility, q the electronic charge, N_C the carrier concentration at equilibrium, E_C–E_F the energy difference between the conduction band and the Fermi level, k the Boltzmann constant, T the absolute temperature. $WO_{x<3}$ is a n-type semiconductor, the transport is metallic for $x < 2.9$ [33]. The stoichiometry of the WO_x layer is not known. The scavenging of oxygen from WO_x by HZO during the annealing confers metallic properties to WO_x and will be further discussed elsewhere. In this work, the LRS is obtained after aligning the ferroelectric polarisation towards the WO_x layer, i.e. when carriers are not accumulated, but depleted in the later. This was already observed for WO_x (3 nm)/HZO (5 nm) devices fabricated in similar conditions [18], where we showed that the resistive switching occurred within the HZO layer, the WO_x layer being considered as a metal.

In this work, the electric field is assumed to drop mainly across the ferroelectric layer (i.e., the thickness t is assumed to be the thickness of HZO, 2.7 nm). For each temperature, the experimental data is fitted in the Log(J+)–Log(V+) representation by a linear regression (solid lines). Figure 5(b) shows the Arrhenius plot of the intercepts of the linear regressions from figure 5(a) (blue data points: LRS, red data points: HRS), as a function of the inverse of the temperature. Again, two linear regressions are performed (solid lines). Using equation (1), the product μN_C (assumed independent of the temperature [34]) and E_C–E_F in the LRS and the HRS can then be estimated. The same analysis is performed for the five devices with varying fatigue states. Independently on the number of cycles, the On/Off ratio, calculated from the difference of the intercepts of the linear regressions in figure 5(a), decreases with temperature (figure 5(c)). For a given temperature, a decrease of the On/Off ratio is observed for the most fatigued device (red curve), along with a decrease of the resistance in the HRS by 20%, compared to the pristine device (green curve). E_C–E_F (squares and circles, left axis) and μN_C (diamonds and pentagons, right axis) parameters are measured in the LRS (blue symbols) and the HRS (red symbols) for different number of cycles. They do not capture an eventual gradient within the HZO layer. In the LRS, E_C–E_F is independent from the fatigue, and equal to 0.28 eV. In the HRS, it is 0.33 eV in the pristine

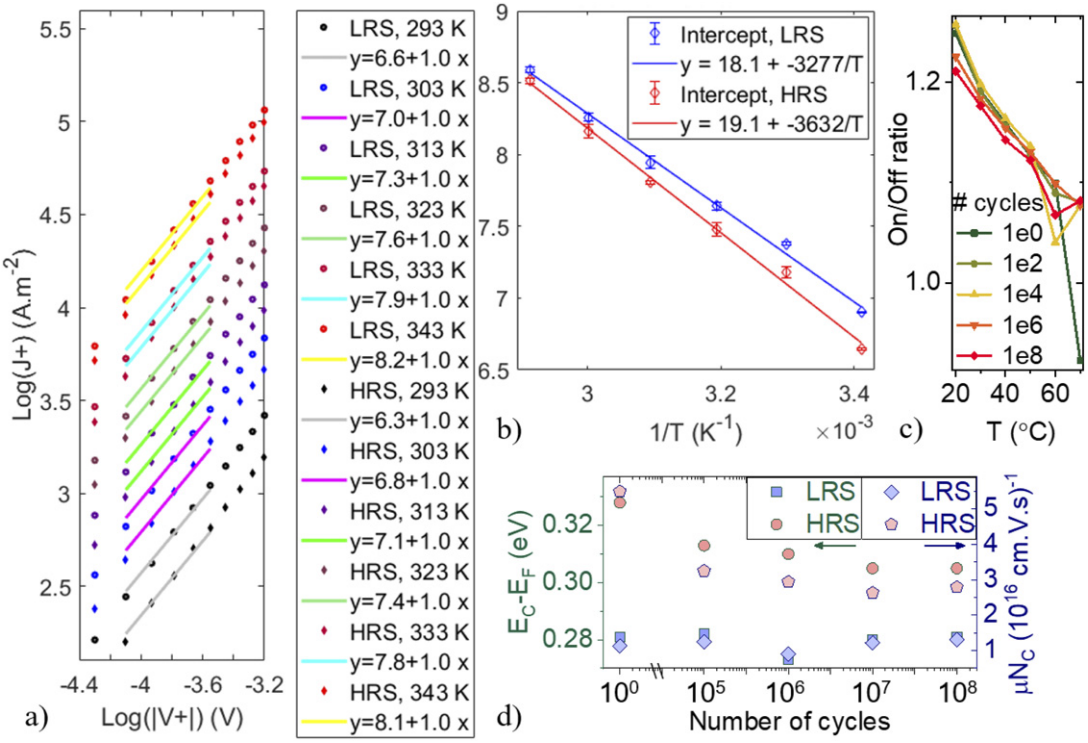

Figure 5. (a) In the Log($J+$) (the current density) as a function of Log($V+$) (the positive bias on the top electrode) representation and for each temperature in the range 393 K–343 K, in the LRS (circles) and in the HRS (diamonds) are fitted by a line of slope 1 (solid lines). The device has a diameter of 40 μm and is fatigued with 10^5 cycles. The Arrhenius plot (b) of the intercepts (blue: LRS, red: HRS) of the regressions is linear. From (b) the E_C–E_F and μN_C parameters can be calculated. Devices with different fatigue states are measured. (c) On/Off as a function of temperature and fatigue (number of cycles). (d) E_C–E_F (squares, circles, left axis) and μN_C (diamonds, pentagons, right axis) parameters are measured in the LRS (blue symbols) and the HRS (red symbols) for different number of cycles.

state, value which decreases gradually with fatigue towards 0.30 eV. These values are relatively small compared to the HZO band gap, which indicate the presence of donor states. The change in E_C–E_F upon switching could be explained by a redistribution of such states, leading to a larger gap in the HRS than in the LRS. Similarly, the product μN_C is independent from the fatigue in the LRS. In the HRS, the product decreases from 5.5 to 2.8 $\times$ 10^{16} (cm V s)$^{-1}$ with fatigue, supporting the scenario of electrostatic redistribution of carriers in the HZO as the polarization switches. Such mechanisms can be driven by the self-screening of the polarization charges, as already seen in semiconducting ferroelectrics [35, 36].

5. Conclusion

Ferroelectric synaptic weights were fabricated based on an ultra-thin (2.7 nm) HZO layer. The crystallization using the millisecond flash-lamp annealing requires a thermal budget of only 500 °C, several hundreds of degrees lower than what is required with the conventional rapid thermal annealing technique. Compared to state-of-the-art 5 nm thick HZO devices, the current density is increased by 10^4. Analog resistive switching is obtained using 20 ns long pulses of increasing amplitude, as well as using +/−1 V pulses of increasing duration. Despite the reduced On/Off compared to devices fabricated with thicker HZO, the stochasticity is very small with a cycle-to-cycle variation below 1%. The synaptic weights are thus good candidates in circuits with low requirements on the dynamic range such as circuits based on differential pairs (see for example [37–39]). The devices have a good endurance, with a limited degradation of the functionality after 10^8 full switching cycles. The analysis of the temperature dependent current–voltage characteristics reveals that HZO can be described as a semi-conductor. As the devices are cycled, the energy difference between the conduction band and the Fermi level, as well as the mobility-carrier density product, decrease. The decay is observed only in the high resistive state, resulting in a reduction of the On/Off ratio upon cycling.

Part of this work was presented at ESSCIRC 2021, see [40].

Acknowledgments

This work is funded by H2020: FREEMIND (No. 840903), ULPEC (No. 732642), BeFerroSynaptic (No. 871737), and UNICO (ANR-19-CHR3-0006). The authors acknowledge the *Binnig and Rohrer Nanotechnology Centre* (*BRNC*).

Data availability statement

The data that support the findings of this study are available upon reasonable request from the authors.

ORCID iDs

Laura Bégon-Lours https://orcid.org/0000-0003-2520-3317
Mattia Halter https://orcid.org/0000-0001-8468-9105
Francesco Maria Puglisi https://orcid.org/0000-0001-6178-2614
Bert Jan Offrein https://orcid.org/0000-0001-6082-0068

References

[1] Sebastian A, Le Gallo M, Khaddam-Aljameh R and Eleftheriou E 2020 Memory devices and applications for in-memory computing *Nat. Nanotechnol.* **15** 529–44
[2] Zhang H, Chen G, Ooi B C, Tan K-L and Zhang M 2015 In-memory big data management and processing: a survey *IEEE Trans. Knowl. Data Eng.* **27** 1920–48
[3] Müller J *et al* 2011 Ferroelectric $Zr_{0.5}Hf_{0.5}O_2$ thin films for nonvolatile memory applications *Appl. Phys. Lett.* **99** 112901
[4] Böscke T S, Müller J, Bräuhaus D, Schröder U and Böttger U 2011 Ferroelectricity in hafnium oxide thin films *Appl. Phys. Lett.* **99** 102903
[5] Garcia V and Bibes M 2014 Ferroelectric tunnel junctions for information storage and processing *Nat. Commun.* **5** 4289
[6] Zhuravlev M Y, Sabirianov R F, Jaswal S S and Tsymbal E Y 2005 Giant electroresistance in ferroelectric tunnel junctions *Phys. Rev. Lett.* **94** 246802
[7] Ma C *et al* 2020 Sub-nanosecond memristor based on ferroelectric tunnel junction *Nat. Commun.* **11** 1439
[8] Stoliar P, Yamada H, Toyosaki Y and Sawa A 2019 Spike-shape dependence of the spike-timing dependent synaptic plasticity in ferroelectric-tunnel-junction synapses *Sci. Rep.* **9** 17740
[9] Wei Y *et al* 2018 A rhombohedral ferroelectric phase in epitaxially strained $Hf_{0.5}Zr_{0.5}O_2$ thin films *Nat. Mater.* **17** 1095–100
[10] Sulzbach M C *et al* 2020 Unraveling ferroelectric polarization and ionic contributions to electroresistance in epitaxial $Hf_{0.5}Zr_{0.5}O_2$ tunnel junctions *Adv. Electron. Mater.* **6** 1900852
[11] Max B, Hoffmann M, Slesazeck S and Mikolajick T 2020 Built-in bias fields for retention stabilisation in hafnia-based ferroelectric tunnel junctions *Electron. Lett.* **56** 1108–10
[12] Fujii S, Yamaguchi M, Kabuyanagi S, Ota K and Saitoh M 2020 Improved state stability of HfO_2 ferroelectric tunnel junction by template-induced crystallization and remote scavenging for efficient in-memory reinforcement learning *2020 IEEE Symp. on VLSI Technology* (Honolulu, HI, USA) pp 1–2
[13] Berdan R, Marukame T, Ota K, Yamaguchi M, Saitoh M, Fujii S, Deguchi J and Nishi Y 2020 Low-power linear computation using nonlinear ferroelectric tunnel junction memristors *Nat. Electron.* **3** 259–66
[14] Bégon-Lours L *et al* 2020 Stabilization of phase-pure rhombohedral $HfZrO_4$ in pulsed laser deposited thin films *Phys. Rev. Mater.* **4** 043401
[15] Ambriz-Vargas F *et al* 2017 A complementary metal oxide semiconductor process-compatible ferroelectric tunnel junction *ACS Appl. Mater. Interfaces* **9** 13262–8
[16] Zacharaki C, Tsipas P, Chaitoglou S, Bégon-Lours L, Halter M and Dimoulas A 2020 Reliability aspects of ferroelectric TiN/$Hf_{0.5}Zr_{0.5}O_2$/Ge capacitors grown by plasma assisted atomic oxygen deposition *Appl. Phys. Lett.* **117** 212905
[17] Tahara K *et al* 2021 Strategy toward HZO BEOL-FeRAM with low-voltage operation ($\leqslant$1.2 V), low process temperature, and high endurance by thickness scaling *2021 Symp. on VLSI Technology* p 2
[18] Begon-Lours L *et al* 2021 Analog resistive switching in BEOL, ferroelectric synaptic weights *IEEE J. Electron Devices Soc.* **9** 1275–81
[19] Bégon-Lours L, Halter M, Popoff Y and Offrein B J 2020 Ferroelectric, analog resistive switching in BEOL compatible TiN/$HfZrO_4$/TiO_x junctions *Phys. Status Solidi* **15** 202000524
[20] Hyuk Park M, Joon Kim H, Jin Kim Y, Moon T and Seong Hwang C 2014 The effects of crystallographic orientation and strain of thin $Hf_{0.5}Zr_{0.5}O_2$ film on its ferroelectricity *Appl. Phys. Lett.* **104** 072901
[21] O'Connor É *et al* 2018 Stabilization of ferroelectric $Hf_xZr_{1-x}O_2$ films using a millisecond flash lamp annealing technique *APL Mater.* **6** 121103
[22] Materlik R, Künneth C and Kersch A 2015 The origin of ferroelectricity in $Hf_{1-x}Zr_xO_2$: a computational investigation and a surface energy model *J. Appl. Phys.* **117** 134109
[23] Müller J *et al* 2012 Ferroelectricity in simple binary ZrO_2 and HfO_2 *Nano Lett.* **12** 4318–23
[24] Warren B E 1990 *X-ray Diffraction* (New York: Dover Publications)
[25] Momma K and Izumi F 2011 VESTA 3 for three-dimensional visualization of crystal, volumetric and morphology data *J. Appl. Crystallogr.* **44** 1272–6
[26] Boyn S *et al* 2017 Learning through ferroelectric domain dynamics in solid-state synapses *Nat. Commun.* **8** 14736
[27] Max B, Hoffmann M, Mulaosmanovic H, Slesazeck S and Mikolajick T 2020 Hafnia-based double-layer ferroelectric tunnel junctions as artificial synapses for neuromorphic computing *ACS Appl. Electron. Mater.* **2** 4023–33

[28] Merz W J 1954 Domain formation and domain wall motions in ferroelectric $BaTiO_3$ single crystals *Phys. Rev.* **95** 690–8
[29] Chernikova A *et al* 2016 Ultrathin $Hf_{0.5}Zr_{0.5}O_2$ ferroelectric films on Si *ACS Appl. Mater. Interfaces* **8** 7232–7
[30] Park M H, Kim H J, Kim Y J, Lee Y H, Moon T, Kim K D, Hyun S D and Hwang C S 2015 Study on the size effect in $Hf_{0.5}Zr_{0.5}O_2$ films thinner than 8 nm before and after wake-up field cycling *Appl. Phys. Lett.* **107** 192907
[31] Junquera J and Ghosez P 2003 Critical thickness for ferroelectricity in perovskite ultrathin films *Nature* **422** 506–9
[32] Lee J, Chiu F and Juan P 2009 *Handbook of Nanoceramics and Their Based Nanodevices* vol 4 (Stevenson Ranch, CA, USA: American Scientific Publishers)
[33] Salje E and Güttler B 1984 Anderson transition and intermediate polaron formation in WO_{3-x} transport properties and optical absorption *Phil. Mag.* B **50** 607–20
[34] Sze S M and Ng K K 2007 *Physics of Semiconductor Devices* 3rd edn (New York: Wiley-Interscience)
[35] Li J *et al* 2019 Giant electroresistance in ferroionic tunnel junctions *iScience* **16** 368–77
[36] Tian B, Bo L, Yang C, Liu F and Wang J L 2015 Space-charge effect on electroresistance in metal-ferroelectric-metal capacitors *Sci. Rep.* **5** 9
[37] Alibart F, Zamanidoost E and Strukov D B 2013 Pattern classification by memristive crossbar circuits using ex situ and *in situ* training *Nat. Commun.* **4** 2072
[38] Prezioso M, Merrikh-Bayat F, Hoskins B D, Adam G C, Likharev K K and Strukov D B 2015 Training and operation of an integrated neuromorphic network based on metal-oxide memristors *Nature* **521** 61–4
[39] Bayat F M, Prezioso M, Chakrabarti B, Nili H, Kataeva I and Strukov D 2018 Implementation of multilayer perceptron network with highly uniform passive memristive crossbar circuits *Nat. Commun.* **9** 2331
[40] Begon-Lours L, Halter M, Popoff Y, Yu Z, Falcone D F and Offrein B J 2021 High-conductance, ohmic-like $HfZrO_4$ ferroelectric memristor *ESSCIRC 2021—IEEE 47th European Solid State Circuits Conf. (ESSCIRC)* (Grenoble, France) pp 87–90